Journal of Manufacturing Processes 156 (2025) 327–341

Contents lists available at ScienceDirect

Journal of Manufacturing Processes

journal homepage: www.elsevier.com/locate/manpro

Full length article

Potential of asymmetric strip tension to control the surface roughness in cold rolling

Christopher Schulte [a,*], Xinyang Li [b], Mengmeng Zhang [b], David Bailly [b], Heike Vallery [a], Sebastian Stemmler [a]

[a] Institute of Automatic Control, RWTH Aachen University, Campus-Boulevard 30, Aachen, 52074, Germany
[b] Institute of Metal Forming, RWTH Aachen University, Intzestrasse 10, Aachen, 52072, Germany

HIGHLIGHTS

- Novel multi-scale model predicts surface imprint with asymmetric strip tension.
- Asymmetric tension independently controls roughness and thickness in single stand configurations.
- Real-time surface measurement enables model-based roughness control in rolling.
- Method can tackle roll wear to keep consistent surface texture across operations.

GRAPHICAL ABSTRACT

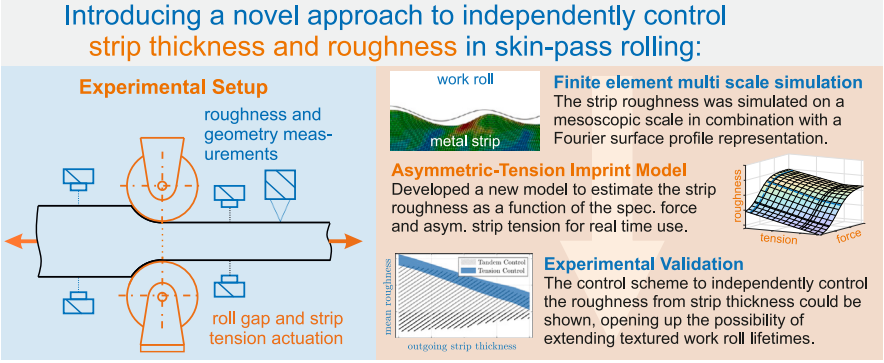

ARTICLE INFO

Dataset link: https://github.com/Don-Chris/data_set_roughness_control_in_cold_rolling

Keywords:
Nonlinear system identification
Cold rolling
Skin-pass rolling
Roughness control
Temper rolling
Surface roughness
FE modeling

ABSTRACT

Accurate control of thickness and surface roughness is becoming increasingly important in the production of metallic strips, as these properties substantially influence downstream processing and product quality. Yet, existing approaches usually focus on only one parameter at a time and thus fall short in demanding industrial environments. We propose a novel methodology for independently controlling both strip thickness and surface roughness in skin-pass rolling by systematically adjusting asymmetric strip tension and roll gap height. We introduce a newly developed Asymmetric-Tension Imprint Model, incorporating specific rolling forces and strip tension that enables accurate real-time roughness prediction. Tests on DC04 steel strips demonstrate the model's accurate prediction of surface roughness with an observational RMSE of 0.202 µm and a noise-reduced RMSE of 0.0973 µm, across an asymmetric tensile stress range up to 158 MPa. Finally, we introduce a new model-based control strategy that simultaneously controls roughness and strip thickness and the concluding validation results highlight the method's industrial potential despite roll wear and fluctuation in strip geometry reducing the control range by 49 % to 67 % compared to simulations.

* Corresponding author.
E-mail address: C.Schulte@irt.rwth-aachen.de (C. Schulte).

https://doi.org/10.1016/j.jmapro.2025.10.081
Received 14 July 2025; Received in revised form 26 September 2025; Accepted 24 October 2025
Available online 7 November 2025

1. Introduction

Requirements for high-quality cold-rolled metal strips extend beyond just precise geometry and outstanding mechanical attributes such as tensile strength, yield strength, and hardness [1]. Surface roughness is important as well, because it largely dictates the optical and tribological properties of the end product. In particular, it correlates with friction coefficients in deep drawing [2] or with glossiness after subsequent painting [3,4].

The temper or skin-pass rolling process, which follows conventional cold rolling and typically involves up to two roll stands, crucially controls strip surface quality [5]. Here, textured rolls are used, to influence the surface of the metallic strip. These rolls are produced via electrical discharge texturing (EDT), or shot-blast texturing. Primarily targeting surface roughness, skin-pass rolling typically employs low rolling forces and thickness reductions between 1 to 5% to avoid unnecessary hardening or altering other product properties [5].

Imprinting texture onto the metallic strip depends on diverse process parameters. Some cannot readily be manipulated, such as initial strip surface, lubrication [6], material strength, roll radius, and work roll surface [7]. Easier to manipulate in a closed-loop fashion are two other determinants of strip surface: roll gap height and strip tension. However, roll gap height simultaneously also influences strip thickness monotonically. Strip tension can influence both the magnitude and the distribution of the contact stresses in the roll gap, thereby affecting surface imprinting. One approach is to apply symmetric strip tension, which primarily alters the overall magnitude of these stresses [8].

To independently control surface roughness from strip thickness adjustments, two distinct approaches have been examined or proposed within both the industrial and research domains. The first approach relies on manipulating symmetric strip tension in combination with roll gap height [8], thus requiring only one roll gap. However, this approach may require strip tension levels exceeding 60% of the material's yield strength, risking tensile tear and contradicting the aim of inducing compressive stresses. Consequently, the maximum strip tension is effectively limited by the material's yield strength and material geometry to operate the system at safe operating points. Additionally, sufficient strip tension is imperative to maintain consistent control over roughness, particularly in the face of disruptions resulting from variations in the incoming strip geometry, strip properties, and wear encountered by the work rolls [9].

The second approach relies on a tandem rolling mill, which simultaneously controls strip roughness and thickness reduction by using two successive passes through work rolls with different textures. This facilitates a broad spectrum of strip roughness within the operational range [9]. Here, an adaptive pass scheduling algorithm typically determines the individual height reductions of the two rolling passes based on the desired strip roughness and strip thickness. In [9], the authors initialized the mathematical relationship inside of the pass scheduling algorithm using established process models and adapted the resulting map online using Gaussian process regression. Using a pair of smooth and rough work rolls, a manipulation of strip roughness of $1.2\,\mu m$ to $2.5\,\mu m$ with an outgoing thickness of $(0.920 \pm 0.008)\,mm$ was achieved for a DC04 steel and an initial geometry ($w_0 \times h_0$) of $8.06 \times 1\,mm$. However, this strategy needs two stands and rolls with varying degrees of surface roughness. Furthermore, each additional pass results in an increase in the minimum adjustable height reduction, to ensure that every stand functions without experiencing strip slip. Additionally, dedicated skin-pass rolling mills are utilized in the industry that only include a single roll stand, which excludes approaches based on pass scheduling algorithms in those cases.

So far, optimization of process parameters has been done almost exclusively off-line. For example, [10] introduced a feed-forward scheduling scheme for a tandem rolling mill to control roughness using a heuristic model based on data from tactile roughness sensors. The model linked parameters like rolling force, roll roughness, and roll radius to strip roughness. This optimization resulted in an average roughness of $(0.42 \pm 0.05)\,\mu m$ for about 65% of the material, whereas without these techniques, this roughness was achieved only 15% of the time. Additionally, assessing the transferability and actual accuracy of the model is challenging, as only 100 measurements of a single material have been conducted, and there is no information on the temporal distribution of the measurements during the experiment.

In another example, a heuristic model was described to forecast strip roughness based on factors such as mean contact stress, roll roughness, and material strength [11]. Experimental validation of that model demonstrated a slight mean deviation of 7% covering a range of strip roughness values ranging from $1\,\mu m$ to $2.5\,\mu m$ across a strip length of $170\,km$. It should be noted, however, that in the experiment only 23 measurements of the resulting roughness were conducted and the chosen set point remained fairly consistent during the experiment, so the reduction in resulting roughness from $2.5\,\mu m$ to $1\,\mu m$ can primarily be attributed to roll wear [11].

Little work has been done in terms of online adaptation of parameters, which would allow closed-loop control. For strip thickness, a framework for high-precision control exists [12,13]: The researchers integrated a piezoelectric stack actuator into the roll stands to increase the dynamics and precision of the roll gap. A rolling force model [14] predicted the thickness of the strip and was identified online using Gaussian process regression [15]. This promising approach, however, is limited by its assumption of Gaussian noise. Consequently, model identification methods utilizing the Huber Loss are attracting interest since it promises robust parameter optimization despite measurement outliers. [16]. In one example, the iteratively-reweighted least squares algorithm has been applied to learn the mill stand curve in cold rolling [17]. In another publication, Huber-Loss was integrated into a Moving Horizon Estimator with sequential quadratic programs for detecting measurement failures [18].

One barrier to closed-loop control of roughness is the availability of sensors that can measure roughness continuously and in real time, during the cold-rolling process. However, such sensors have become available in the recent past, primarily based on a light-section method [19]. These sensors now enable real-time roughness measurements, as a prerequisite for closed-loop control.

In this work, we present a third and alternative approach for simultaneous closed-loop control of thickness and roughness, by leveraging asymmetric strip tension in a single roll stand, which can additionally shift the distribution of the contact stresses. Firstly, this approach offers the advantage that only one roll stand is needed for operation, similar to the approach presented by [11]. Secondly, the influence of the strip tension actuators on the controlled variables is further improved by focusing on the movement of the non-slip (neutral) point inside the roll gap.

Building on this, the present work makes the following contributions:

1. We improve an existing multiscale modeling framework by employing an optimized Fourier-based surface profile representation of the work roll that preserves Ra, RPc, and key Abbot-Firestone curve percentiles, yielding predictive confidence bands (Section 3).
2. We propose the Asymmetric-Tension Imprint Model (ATIM), which augments a validated imprint formulation with specific force and specific tension offset as inputs. We provide a transparent parameter identification scheme with explicit objective, bounds, and data volume (Section 4).
3. We establish a model-based control strategy that uses the ATIM with a cold-rolling force model and a roll-stand deflection model to compute roll gap height and tension settings, quantify the achievable process window, and derive actuator-rate requirements for disturbance rejection (Sections 5.1 and 5.2).

4. We present an experimental process analysis of the presented control strategy and report both observational and noise-reduced accuracy metrics. We also analyze how roll wear and incoming-geometry variability constrain the feasible process window in practice (Section 5.3).

2. Problem statement and existing model

2.1. Problem statement

A fundamental challenge in rolling operations is to effectively capture and analyze key process variables, such as strip thickness and surface roughness, within the roll gap. Direct measurement of these parameters is often limited by design constraints, making it necessary to position most sensors outside the roll gap, in addition to the load cell measuring rolling force.

Because of these constraints, a frequently used and straightforward approach to studying this multi-objective control problem is to employ a single roll stand equipped with strip tension actuators. This setup provides a controlled and simplified environment for investigating how variations in strip geometry, rolling force, and strip tension affect the final product, even when in-gap measurements are not feasible. By examining process behavior under these conditions, researchers can gain insights into fundamental rolling dynamics and develop methods that can be transferred or adapted to more complex systems. The diagram presented in Fig. 1 illustrates the structural configuration of the experimental setup. As mentioned, design constraints prevent direct measurement of process variables such as strip thickness h_1 and surface roughness Ra in the roll gap. Consequently, all sensors, except the load cell measuring rolling force F inside the stand, are placed outside the roll gap.

The separation of spatial arrangement is beneficial when considering the measurement of thickness $h_{0,\mathrm{m}}$ and width $w_{0,\mathrm{m}}$. This is particularly notable because it allows for a simple buffering topology characterized by lengths l_{h_0} and l_{w_0} and strip speed v_0, aiding in determining the roll gap's current and future thickness h_0 and width w_0 [12].

However, positioning the second thickness gauge and roughness sensor at the trailing end results in an inevitable measurement delay depending on both the strip speed v_1 and the associated distances, namely distance between the roll gap and outgoing thickness sensor l_{h_1} and roughness sensor l_{Ra}. Considerable constraints emerge when employing these signals as feedback for control purposes. These constraints are affected by the speed-dependent time delay in the measurements, such as the measured thickness $h_{1,\mathrm{m}}$ and roughness Ra_{m}.

The cold rolling mill can be influenced by three process variables during operation. Firstly, the roll gap height s sets the distance between the rollers. Secondly, the strip tension at the inlet t_0 and at the outlet t_1 can be adjusted.

To address performance and stability limitations, we use a model-based approach. Here, process models estimate time-delayed variables using process variables measured in the roll gap (F), recorded in advance due to transport (h_0, w_0), or actuator values (s, t_0, t_1). Additionally, we adapt these process models online to ensure that the estimated process variables converge to the measured process variables. To achieve this, all relevant input and output variables of the models must be recorded and synchronized online, as discussed in [12].

2.2. Imprint Model

The Imprint Model predicts the roll surface's imprint on the resulting strip's mean roughness. An exploratory analysis described in [20] has demonstrated that the mean strip surface roughness Ra is primarily influenced by the average contact pressure

$$\sigma = \frac{F}{w_0\, l_{\mathrm{c}}} \quad . \tag{1}$$

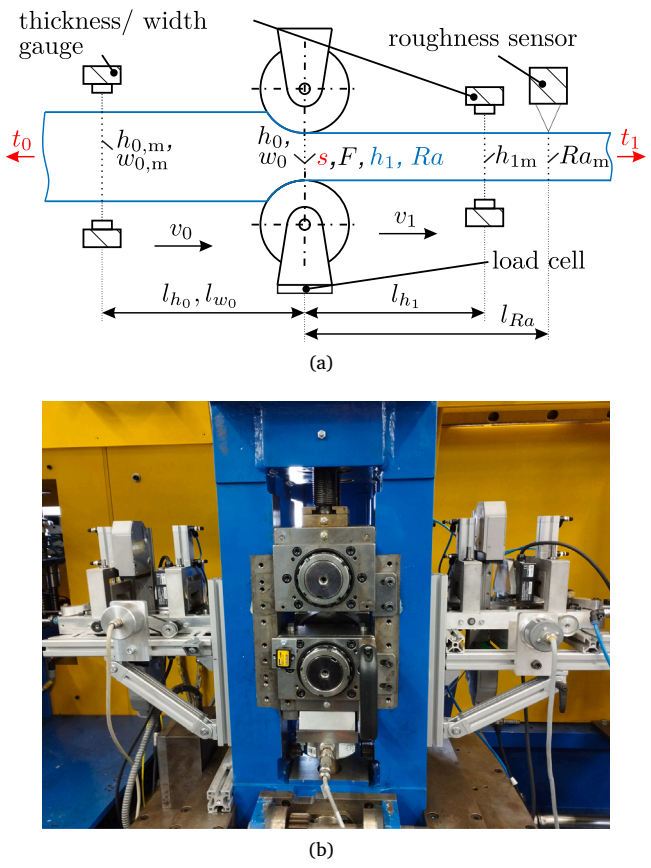

Fig. 1. Rolling mill (a) with thickness and width gauges and incremental encoders to track measured thicknesses to the roll gap. The process variables h_0, w_0, h_1, Ra have two versions: one without a time delay and another with a time delay, indicated by the subscript 'm', adapted from [15]. Additionally, a photo of the experimental roll stand (b) is shown with the roughness sensor not depicted.

The contact area between the roll and the strip is approximated by the area obtained from the contact length l_{c} and material width w_0, assuming that the material does not experience widening. The contact length l_{c} is a critical parameter, although not directly measurable. However, the contact length l_{c} increases monotonically with the reduction of the roll gap for sufficiently small forces during roll engagement. Therefore, the specific rolling force F' can be used as an alternative to contact pressure that is the contact force F scaled by the material width w_0:

$$F' = \frac{F}{w_0} \quad . \tag{2}$$

As first presented in [20], the resulting surface roughness Ra can be modeled empirically as a scaled sigmoid function $f_{\mathrm{I}}(F', \boldsymbol{\Theta}_{\mathrm{I}})$. The Imprint Model is therefore dependent on the specific rolling force F' and additional process parameters $\boldsymbol{\Theta}_{\mathrm{I}}$ consisting of the incoming roughness Ra_{init}, roughness of the working roll Ra_{roll}, over-imprinting factor C_{roll} and specific rolling force F'_{90} at which 90% of the roll roughness is imprinted onto the metallic strip (cf. Table 1):

$$Ra = f_{\mathrm{I}}(F', \boldsymbol{\Theta}_{\mathrm{I}}) = Ra_{\mathrm{init}} + \tag{3}$$

$$\underbrace{\frac{1}{1+\mathrm{e}^{-x}}}_{\mathrm{sig}(x)} \cdot \left(C_{\mathrm{roll}}\, Ra_{\mathrm{roll}} - Ra_{\mathrm{init}}\right) \quad , \tag{4}$$

$$x = \left(\frac{9}{4}\frac{F'}{F'_{90}} - \frac{5}{4}\right) \cdot \ln(9) \quad . \tag{5}$$

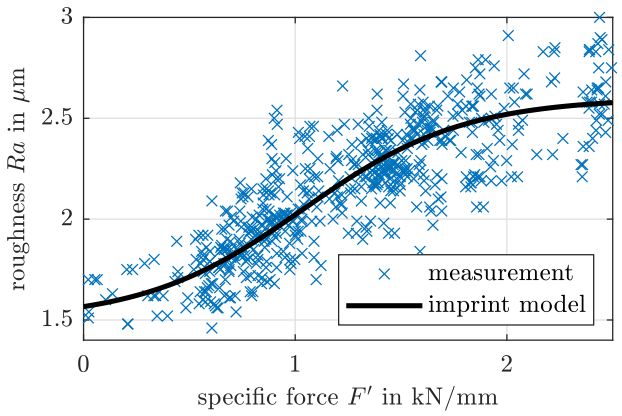

Fig. 2. Identified Imprint Model with rough work rolls, reproduced from [20] with constant tension $t_0 = t_1 = 200\,\mathrm{N}$.

Table 1
Model parameters of the Imprint Model $\boldsymbol{\Theta}_\mathrm{I}$, compare [20].

Variable	Description	Value
Ra_init	Incoming strip roughness	1.5 µm
Ra_roll	Work roll roughness	2.38 µm
F'_{90}	Specific force at 90% imprint	1.99 kN mm^{-1}
C_roll	Factor over-imprinting	1.11

Fig. 2 shows the validated Imprint Model with constant symmetric strip tension of a roll stand with rough work rolls. For low forces, the model converges to the initial roughness Ra_init and for high forces, the model converges to the maximal transferable roughness $Ra_\mathrm{max} = C_\mathrm{roll}\,Ra_\mathrm{roll}$. The factor C_roll was introduced because both simulations and experiments indicated that the strip can achieve roughness greater than that of the work rolls. We hypothesize that this phenomenon may be due to the relative motion between the roll and the strip, leading to the accumulation of peaks on the strip's surface.

Although this approach accurately models the case of symmetrical strip tension, it falls short when trying to predict the strip roughness under varying and asymmetric strip tension, as it assumes no direct influence of the strip tension and neglects the influence of the stress distribution on the resulting strip roughness.

3. Multiscale FE-simulation

3.1. Simulative approach

We choose the Finite element method (FEM) to simulate the surface imprinting during skin-pass rolling with asymmetric strip tension because existing models do not yet have the capability to predict the surface roughness in these conditions. However, the substantial scale difference between the roll diameter and the surface asperities presents a considerable challenge for FEM, particularly in terms of meshing and computational requirements.

To reduce the computing effort, previously developed and extended a multiscale approach is used as a starting point [21]. This approach splits the simulation into two distinct scales: A macroscopic process model and a mesoscopic imprint model that incorporates realistic asperity profiles. Fig. 3 illustrates the complexity of the rolling process and the chosen hierarchical modeling structure.

The macroscopic level (Abaqus/ Standard 6.12 by Dassault Systèmes, headquarter in Vélizy-Villacoublay, France) includes three key elements that collectively define the rolling process on this scale: Roll dimensions, thickness reduction, and strip tension. The roll dimensions remain constant throughout the process, however force-dependent roll flattening is accounted for. The thickness reduction of the materials being processed can vary according to specific process requirements, and the newly introduced asymmetric strip tension can also be adjusted to suit different operational needs.

The macroscopic model provides the boundary conditions for the mesoscopic model (Abaqus/Explicit 6.12), namely the local kinematics between the roll and the workpiece and the stress field within the roll gap. Surface roughness is exclusively modeled at the mesoscopic scale, allowing imprinting results to be obtained from this simulation. To eliminate the influence of element size on the resulting strip roughness, a convergence analysis is performed with element sizes ranging from 0.5 µm to 5 µm at a thickness reduction of 4% for DC04 steel under a symmetric tension of 200 N. The model converges at an element size of 2.0 µm. Considering the tolerance for varying strip tensions and the computational cost, we adopt an element size of 1 µm for the mesoscopic model. For a detailed investigation of the element size selection in the simulation of skin-pass rolling, please refer to [22].

This hierarchical simulation enables studying the influence of asymmetric strip tension on imprinting, without neglecting the tension distributions and relative motion between the roll and the strip. As simulatively shown in [5], an asymmetric strip tension, defined as a difference in strip tension between the outlet and inlet of the rolling stand, has a more pronounced effect on the final strip roughness than symmetric strip tension. For this reason, in this publication we will use the so-called specific tension offset $\Delta t'$, which is the difference between the tension at the outlet t_1 and the tension at the inlet t_0, scaled by the strip width w_0:

$$\Delta t' = \frac{t_1 - t_0}{w_0} \quad . \tag{6}$$

Previous research has also indicated that the resulting roughness of the imprinted strip surface Ra exhibits a (non-Gaussian) distribution within a specified range. Measurement noise contributes only marginally, as substantial process variations can still be observed even after multiple measurements of the same rolled strip. One of the reasons for this can be the stochastic asperity introduced by EDT, which cannot be adequately represented by the deterministic sine curves employed in the mesoscopic model so far [21].

To address this issue, we incorporate a more realistic surface profile that accurately captures the stochastic nature of the asperities introduced by EDT. This will not only improve the representation of surface roughness, but will also lead to more reliable results for the peak number RPc, which is vital for enhancing the precision of mesoscopic simulations.

3.2. Surface profile generation

In order to create a more realistic surface profile representation in the mesoscopic model, we introduce a new representation based on the Fourier series. This surface profile representation $f_\mathrm{F}(l, \Theta_\mathrm{F})$ depends on Fourier parameters Θ_F of Fourier order n_max, which are optimized to fit a given surface mean roughness Ra, peak count RPc, [23] and the Abbott-Firestone curve [24].

The Abbott-Firestone curve (AFC) $\Lambda = f_\Lambda(p_\mathrm{v})$, also known as the material ratio curve, is a function of the volume fraction p_v and characterizes the surface texture of an object by analyzing the profile trace $f_\mathrm{F}(l, \Theta_\mathrm{F})$ along the length of the strip l. This curve is derived by drawing lines parallel to a datum and measuring the portion of the volume within the profile. Mathematically, it represents the cumulative probability density function of the surface profile's height, calculated through the integration of the probability density function ([25], p.407).

To determine the deviation between the measured and optimized Abbott-Firestone Curve (Λ), the curve is evaluated at three predetermined positions $p_\mathrm{v} = [5\%, 50\%, 95\%]$ (Λ_5, Λ_{50}, and Λ_{95}, see Fig. 4).

The developed cost function then penalizes the deviation between the measured and optimized surface texture parameters Θ_S =

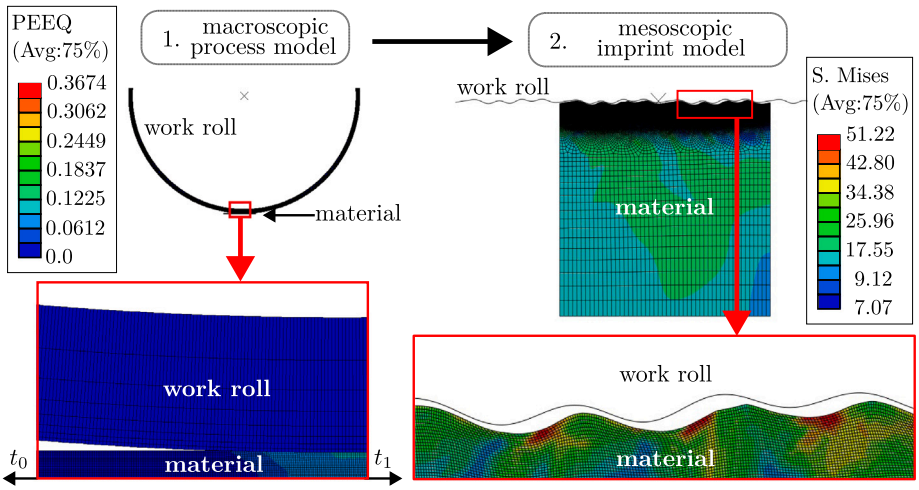

Fig. 3. Overview of the two step finite element simulation. First the macroscopic process simulation to calculate the boundary conditions that are then applied in the mesoscopic imprint simulation. Shown is an example simulation with Equivalent Plastic Strain (PEEQ) and von Mises stress (S. Mises) in the mesoscopic simulation.

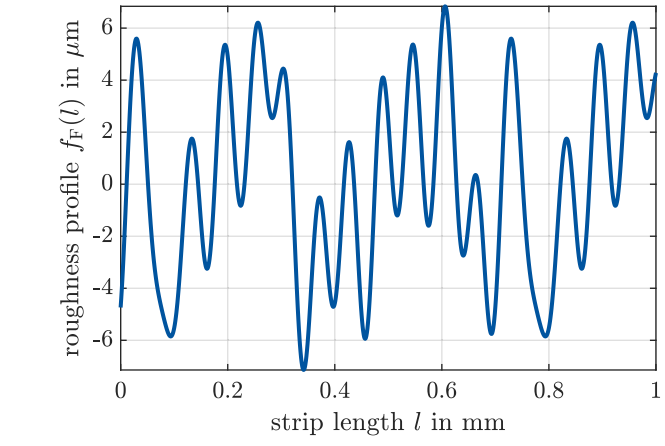

(a)

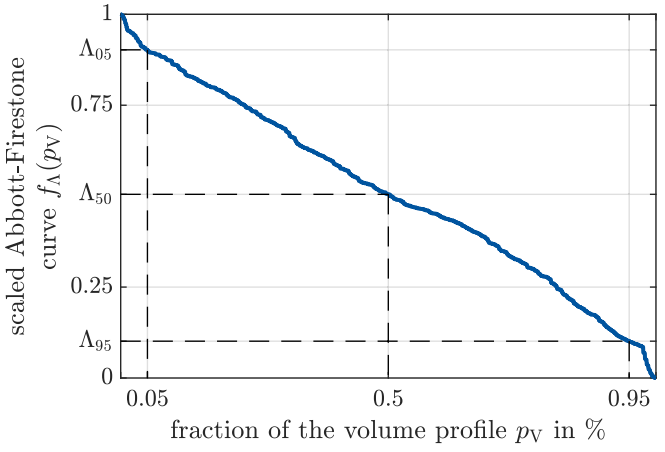

(b)

Fig. 4. The Abbott-Firestone curve (a) of an example surface profile (b) that was generated using the proposed Fourier series representation.

$[Ra, RPc, \Lambda_5, \Lambda_{50}, \Lambda_{95}]$, consisting of the three Abbot-Firestone values Λ, the surface mean roughness, and peak count.

To minimize this cost function, a black-box optimization is used that does not rely on an algebraic derivative of the cost function. One reason why determining the derivative is not possible is the calculation of the peak count RPc, which is based on the number of peaks in a given roughness profile that exceed a certain threshold above the mean profile height [23].

For this reason, Nelder–Mead particle swarm optimization (NM-PSO) is used [26], which is a combination of the Nelder–Mead simplex method [27] and particle swarm optimization (PSO) [28]. The Nelder–Mead simplex method is a direct search method for nonlinear optimization problems, which is based on the concept of a simplex, a generalization of intervals and triangles to arbitrary dimensions. The PSO is a population-based stochastic optimization technique inspired by the social behavior of flocking birds or schooling fish [28]. In this algorithm, each candidate solution is a particle, and these particles move through the problem space, following the current optimum particles.

The NM-PSO algorithm is implemented in MATLAB and the optimization problem is formulated as follows and the surface parameters Θ_S, the desired surface parameters $\Theta_{S,des}$, Fourier parameters Θ_F with minimal $\Theta_{F,min}$ and maximal value $\Theta_{F,max}$ are summarized in Table 2. The calculation of the surface texture parameters Θ_S as a function of the surface profile representation $f_F(l, \Theta_F)$ is based on the definition in ISO 21920-2 [23]:

$$\begin{aligned} \min_{\Theta_F} \quad & \|\Theta_S - \Theta_{S,des}\|_Q^2 \\ \text{s.t.} \quad & \Theta_{F,min} < \Theta_F < \Theta_{F,max} \\ & f_F(l, \Theta_F) = \sum_{i=1}^{n_{max}} \left(a_i \cos\left(\omega_0\, i\, l\right) + b_i \sin\left(\omega_0\, i\, l\right)\right) \\ & \Theta_F = \left[a_1, \ldots, a_{n_{max}}, b_1, \ldots, b_{n_{max}}, \omega_0\right] \end{aligned} \tag{7}$$

We can use this optimization to generate different surface profile representations $f_F(l, \Theta_F)$ while achieving the same final surface parameters Θ_S. We consider these surface profiles as equivalent profiles regarding the mesoscopic simulations, as shown in Fig. 5(a).

Then, we perform mesoscopic simulations for each work roll surface profile and analyze the resulting strip surface. Each roll surface profile yields a different strip roughness even though the roll surface parameters Θ_S were the same. This initially problematic phenomenon is beneficial for assessing simulation uncertainty as shown in the next Section.

Table 2
A comprehensive list of all surface parameters $\Theta_S = \{Ra, RPc, \Lambda_5, \Lambda_{50}, \Lambda_{95}\}$, their desired values $\Theta_{S,des}$, and the corresponding weights Q that were used for the optimization of a surface profile representation and an overview of the optimized Fourier series parameters Θ_F and their corresponding limits $\Theta_{F,min}$ and $\Theta_{F,max}$.

	Description	$\Theta_{S,des,i}$	Unit	Q_i
Ra	Mean roughness	2.38	µm	5
RPc	Peak count	80	1/cm	0.2
Λ_5	AFC value at 5%	0.1	–	100
Λ_{50}	AFC value at 50%	0.5	–	20
Λ_{95}	AFC value at 95%	0.9	–	100

	Description	$\Theta_{F,min,i}$	$\Theta_{F,max,i}$
a_i	Fourier series parameter for sin	−2	2
b_i	Fourier series parameter for cos	−2	2
ω_0	Base frequency of the fourier series	0.1	2

3.3. Experimental validation of mesoscopic simulation

We validate this new simulation procedure for the mesoscopic model using a laboratory strip rolling mill by BUEHLER REDEX GmbH (headquartered in Pforzheim, Germany) in a 2-high configuration with a maximum rolling force of 100 kN. In this laboratory set-up, the work rolls have a radius of 75 mm, and both work rolls are textured by EDT. To regulate the roll gap of the mill, a previously developed Model Predictive Controller (MPC) is deployed [12]. The MPC controls the rolling mill's piezoelectric actuators and a conventional spindle actuator, and it compensates for actuator dynamics and potential hysteresis effects. This compensation enables precise tracking of a predetermined roll gap height trajectory. This system ensures a consistent final strip thickness throughout the rolling process [17].

In the validation experiments, DC04 steel with an initial geometry of 8.06×1.02 mm ($w_0 \times h_0$) was considered first. The work rolls used in this validation exhibits a mean surface roughness Ra_{roll} of 2.38 µm and a peak count RPc of 80 cm^{-1}. Roll roughness values were determined using replica rubber mold of the roll surface and analyzed with a Keyence VHX-7000 digital microscope. In the simulation, we used five different surface profile representations from Section 3.2 with the same surface parameters Θ_S (Table 2) in the mesoscopic simulation, see Fig. 5(a). Although these surface profile representations have the same mean roughness, peak count and AFC, they lead to different roughness of the simulated metal strip. We will utilize this ambiguity further to better estimate the uncertainty of the simulation. The initial roughness of the cold-rolled strip is considered flat. This is justified by the substantial roughness difference between the roll and strip surfaces, which makes the initial strip roughness negligible in the simulation [21].

To validate the multi-scale simulations for DC04 steel, we conducted experiments at a thickness reduction of 4%, applying variable specific tension offsets $\Delta t'$ of -25 N mm^{-1}, 0 N mm^{-1}, and 124 N mm^{-1}. We used no lubrication and calculated the friction coefficient to 0.426 by parameter optimization of the Bland and Ford model with the experimental data [21].

The measured and predicted Ra in skin-pass rolling are shown in Fig. 5(b). The simulation results, obtained from different equivalent surface profile representations, define a confidence interval. We can observe high standard deviations in the experimentally measured roughness. However, within the range that can be assessed experimentally, it can be concluded that the mesoscopic simulation shows good agreement with the experimental data.

To further investigate the validity and generality of the model, we also tested DC05 steel with an initial geometry of 8.20×1.02 mm ($w_0 \times h_0$). Furthermore, we used newly textured work rolls with mean roughness Ra_{roll} of 2.30 µm and peak count RPc of 65 cm^{-1} for this validation test. Based on the roll surface profile measured with a Keyence VHX-7000 digital microscope, we determined the parameters for AFC (Λ_5, Λ_{50}, Λ_{95}) as 0.2, 0.5, and 0.8, respectively. Accordingly, we generated five equivalent surface profile representations, each exhibiting the same mean roughness, peak count, and AFC parameters, and employed them in the mesoscopic model (see Fig. 6(a)). Here, we inversely identified the friction coefficient as 0.15.

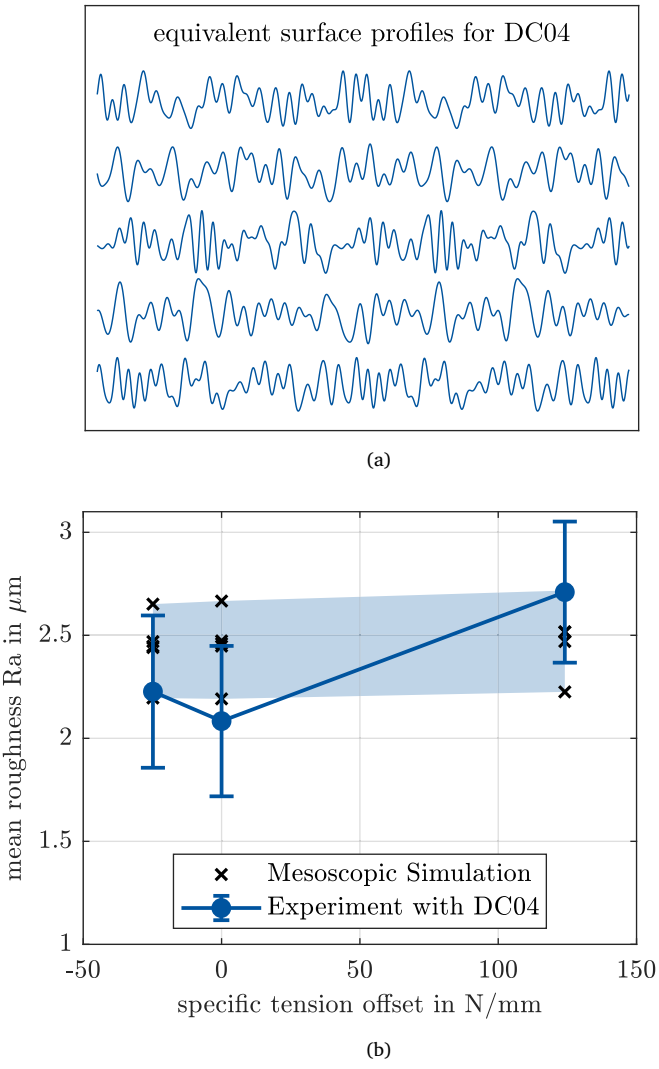

Fig. 5. Equivalent profiles with $Ra = 2.38$ µm, $RPc = 80$ 1/cm, and measured Abbott-Firestone curve (a); validation of mesoscopic model for DC04 steel with respect to Ra (b)

We carried out the validation tests for DC05 under variable specific strip tension offsets $\Delta t'$ of -31 N mm^{-1}, 0 N mm^{-1}, and 122 N mm^{-1} at a thickness reduction of 2%. The comparison between the measured and simulated roughness is shown in Fig. 6(b). The results show good agreement, with the measured roughness lying within the confidence interval of the simulations. This confirms the strong predictive capability of the multiscale simulations for roughness transfer in skin-pass rolling.

However, it should be noted that, due to deviations introduced by the different surface profile representations, the effect of asymmetric strip tensions is not clearly visible in Figs. 5 and 6. To elucidate the influence of asymmetric tension, we carried out additional simulations for DC04 steel at thickness reductions of 2%, 4%, 6%, and 8% with specific tension offsets $\Delta t'$ of -25 N mm^{-1} and 124 N mm^{-1}, respectively.

The predicted roughness and specific rolling force F' from these simulations are presented in Fig. 7. The results indicate that, as the

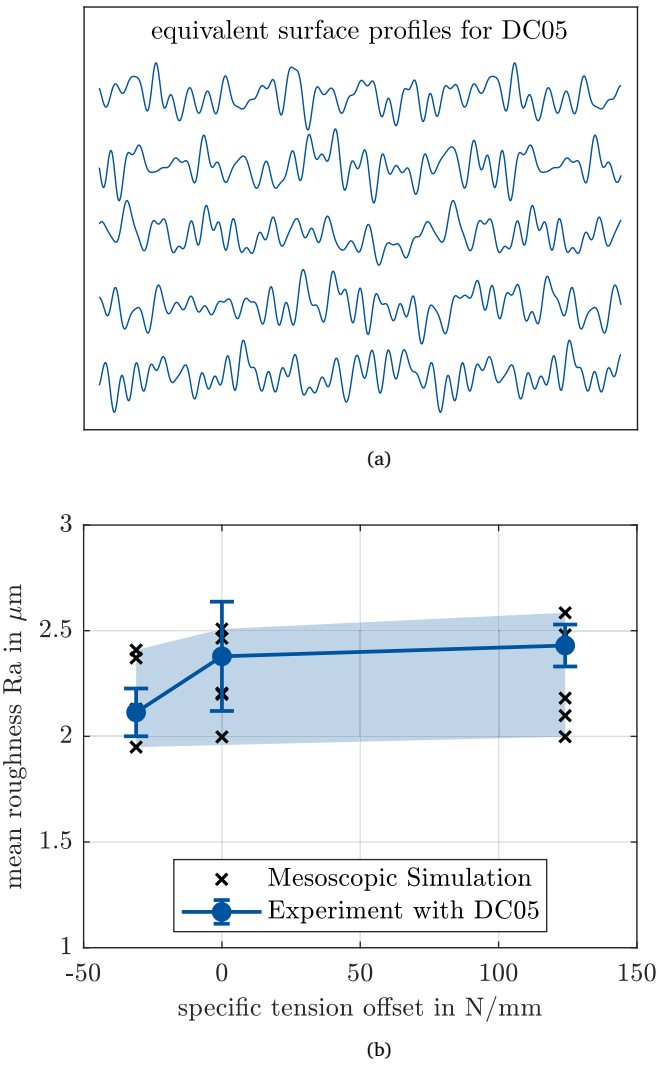

Fig. 6. Equivalent profiles with $Ra = 2.3\,\mu m$, $RPc = 65\,1/cm$, and measured Abbott-Firestone curve (c); and validation of mesoscopic model for DC05 steel (d). All error bars are one standard deviation.

thickness reduction or specific rolling force F' increases, the achievable roughness initially rises sharply and then levels off due to the physical limitation of the roll profile. Furthermore, the comparison of the average lines of the resulting roughness for the two tension conditions shows that an increase in forward tension, corresponding to the specific tension offset of $124\,N\,mm^{-1}$, leads to a higher resulting roughness. This finding implies that applying asymmetric strip tension enhances the controllability of roughness transfer while maintaining the final strip thickness.

4. Asymmetric-Tension Imprint Model

4.1. Modeling approach

The results of the FE simulation have led to the expansion of the existing Imprint Model to account for a direct influence of asymmetric strip tension. Consequently, we modify the previously developed Imprint Model (Section 2.2) by adding the specific strip tension offset $\Delta t'$ as an additional input for what is now referred to as the Asymmetric-Tension Imprint Model (ATIM).

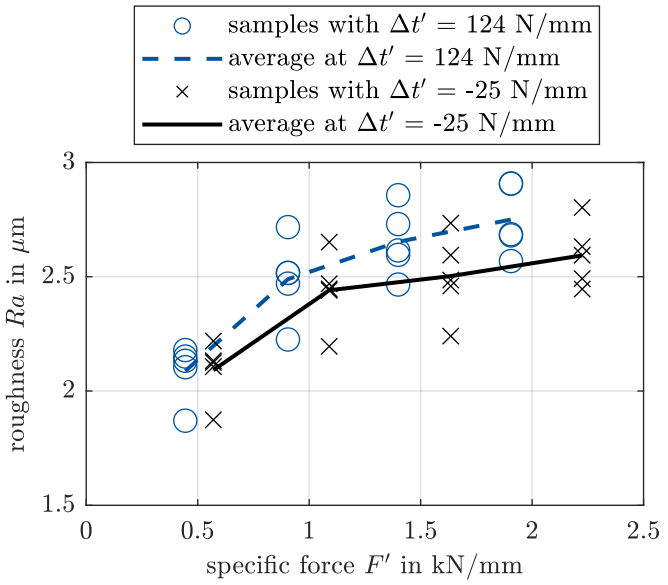

Fig. 7. Simulative results of the mesoscopic model for DC04 with a specific tension offset $\Delta t'$ of $-25\,N\,mm^{-1}$ and $124\,N\,mm^{-1}$.

Based on simulation results of the previous Section, we determined that a set of parameters of the original Imprint Model exists for each specific strip tension offset $\Delta t'$ that estimates the resulting mean roughness to be sufficiently accurate (compare Fig. 7). Therefore, we replace the previously defined model parameters Ra_{init}, Ra_{roll} and F'_{90} from the original Imprint Model (see (4)–(5)) by (linear) functions

$$\begin{aligned} Ra_{init} &= Ra_{init,0} + \Delta Ra_{init} \cdot \Delta t' \\ Ra_{roll} &= Ra_{roll,0} + \Delta Ra_{roll} \cdot |\Delta t'| \\ F'_{90} &= F'_{90,0} + \Delta F'_{90} \cdot \Delta t' \end{aligned} \quad , \tag{8}$$

that depend on the specific strip tension offset $\Delta t'$, the initial values of the respective parameters $Ra_{init,0}$, $Ra_{roll,0}$ and $F'_{90,0}$ and (linear) coefficients ΔRa_{init}, ΔRa_{roll} and $\Delta F'_{90}$ to create the ATIM, compare Table 3:

$$Ra = f_{ti}(F', \Delta t', \boldsymbol{\Theta}_{ti}) \quad . \tag{9}$$

After calculating the intermediate model parameters Ra_{init}, Ra_{roll}, F'_{90} with (8), we calculate the resulting mean roughness of the strip with the original Imprint Model described in (4)–(5). However, given that the specific rolling force F' and tension offset $\Delta t'$ are our model inputs rather than the actual actuator signals themselves, this model is not sufficient to control the roughness itself. Thus, a combination of various models is necessary, a topic we explored further in Section 5.

4.2. Parameterization of the modeling approach

To parameterize the ATIM, we performed a series of experiments on a cold rolling mill. We conducted the experiments using a DC04 steel strip with an initial geometry of $8.06 \times 1\,mm$ ($w_0 \times h_0$). The strip has an initial mean roughness of $(1.5 \pm 0.1)\,\mu m$ and the roughness of the work roll is $2.38\,\mu m$. We varied the specific strip tension offset $\Delta t'$ between $-55\,N\,mm^{-1}$ and $160\,N\,mm^{-1}$ in steps of $6\,N\,mm^{-1}$ to $12\,N\,mm^{-1}$ and continuously increased the specific force F' in the range of $0.5\,kN\,mm^{-1}$ and $2.5\,kN\,mm^{-1}$. After subsequent synchronization of the measurement data due to the different position-based delays, we end up with a total of 3975 data pairs.

To ensure smooth operation of the cold rolling mill and hinder defects, both strip tensions t_0, t_1 should not be lower than 200 N. Additionally the maximum tension at the inlet t_0 is 600 N and the

Table 3
A list of all model parameters Θ_{ti} of the ATIM.

Variable	Description	Value	Unit	$\Theta_{opt,min,i}$	$\Theta_{opt,max,i}$
$Ra_{init,0}$	Incoming strip roughness for $\Delta t' = 0$	1.5	µm	–	–
$Ra_{roll,0}$	Work roll roughness for $\Delta t' = 0$	2.38	µm	–	–
$F'_{90,0}$	Spec. force at 90% imprint for $\Delta t' = 0$	1.99	kN mm^{-1}	–	–
C_{roll}	Factor over-imprinting	1.11	–	–	–
ΔRa_{init}	Rate of change of Ra_{init}	2.7069	µm^2/N	−10	10
ΔRa_{roll}	Rate of change of Ra_{roll}	2.1786	µm^2/N	−10	10
$\Delta F'_{90}$	Rate of change of F'_{90}	1.7555	–	−10	10

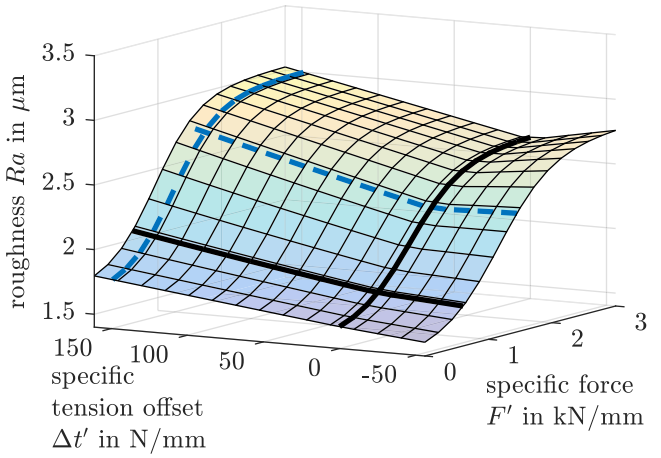

Fig. 8. The Asymmetric-Tension Imprint Model (ATIM) as a 3D map of the input variables specific tension offset and specific force. The depicted lines are shown in more detail in Figs. 9 and 10.

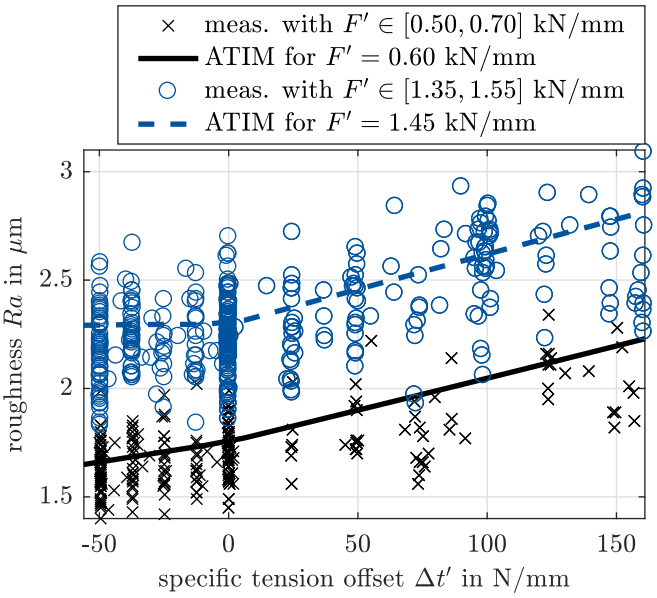

Fig. 9. Evaluation of the Asymmetric-Tension Imprint Model (ATIM) for a constant specific force of 0.6 kN mm^{-1} and 1.45 kN mm^{-1} respectively. Furthermore, the measurement points are shown, which are within a range of ±0.1 kN mm^{-1} of these values.

maximum tension at the outlet t_1 is 1500 N. This corresponds to 35% and 88% of the yield strength of the material at the initial geometry:

$$t_0 = \begin{cases} 200\,\mathrm{N} - \Delta t'\, w_0 & , \Delta t' < 0 \\ 200\,\mathrm{N} & , \Delta t' \geq 0 \end{cases}, \tag{10}$$

$$t_1 = \begin{cases} 200\,\mathrm{N} & , \Delta t' < 0 \\ 200\,\mathrm{N} + \Delta t'\, w_0 & , \Delta t' \geq 0 \end{cases}. \tag{11}$$

To determine the newly introduced model parameters Θ_{opt} based on the acquired data from these experiments, we used the NM-PSO algorithm to minimize the quadratic deviation between the measured roughness and ATIM estimation, see Table 3:

$$\begin{aligned} \min_{\Theta_{opt}} \quad & \left\| Ra_{meas} - Ra \right\|^2 \\ \text{s.t.} \quad & \Theta_{opt,min} < \Theta_{opt} < \Theta_{opt,max} \\ & Ra = f_{ti}(F', \Delta t', \Theta_{ti}) \\ & \Theta_{opt} = \left[\Delta Ra_{init}, \Delta Ra_{roll}, \Delta F'_{90} \right] \end{aligned} \tag{12}$$

Fig. 8 shows the three-dimensional ATIM without measurements to improve visibility. The inputs are the specific strip tension offset $\Delta t'$ and specific force F' and these are shown within ranges −55 N mm^{-1} to 160 N mm^{-1} and 0 kN mm^{-1} to 3 kN mm^{-1}, respectively. Higher strip tension is not technically achievable with this rolling mill, and forces over 3 kN mm^{-1} are not needed for the skin-pass rolling process, as they transfer the roll roughness to the strip fully.

The ATIM shows a noticeable discontinuity at offset $\Delta t' = 0$, where the specific strip tension is at its minimum ($t_0 = t_1 = 200$ N). For negative offset $\Delta t'$, the tension at the inlet t_0 increases. For positive offset $\Delta t'$, the tension at the outlet t_1 increases. Consequently, the energy transferred via the tension of the strip is lowest at $\Delta t' = 0$ and increases for both negative and positive $\Delta t'$. The mean roughness of the strip increases with increasing specific tension offset $\Delta t'$ due to a greater reduction in height under the same specific force F'.

Furthermore, the predictions of the model are illustrated by two sets of parallel lines along a specific force or tension offset, each representing one of the inputs held constant. These sets of lines are further detailed in Figs. 9 and 10 along with all measurement points within the region of the fixed input (±0.1 kN mm^{-1} and ±1 N mm^{-1} respectively).

To visualize the model accuracy across the entire working range of the specific force and tension offset, we divided ATIM into a grid based on the two input parameters F' and $\Delta t'$, see Fig. 11. Subsequently, we calculated the root mean square error (RMSE) between the predictions of the model and the measurement data in each element of the grid. We indicated the RMSE corresponding to each grid element by its color.

To prevent strip slip in the roll gap, a minimum force of 0.5 kN mm^{-1} is required for all specific strip tension offsets $|\Delta t'| > 12$ N mm^{-1}. This explains the missing boxes on the left side of the Figure. Furthermore, four combinations of process parameters stand out that did not occur in the experiment.

To provide a clearer interpretation of the results, we take a closer look at the measurement noise of the roughness sensor. The manufacturer explains that the measuring head's uncertainty is 0.008 µm, based on a roughness standard with $Ra = 1.27$ µm. This considers laser power fluctuation, stray light noise, temperature control behavior, and camera chip noise, but excludes ventilation vibrations and ambient light disturbances. In a determination of the measurement uncertainty budget according to GUM or EU Directive EAL-R4, the manufacturer specifies a total measurement noise of 0.103 µm for the roughness standard used in the investigation [29]. However, since the measurement noise also depends on the reflectivity of the surface, an influence of the material and surface properties on the measurement noise cannot be excluded. Fan-induced vibrations can already lead to fluctuations in the measurement

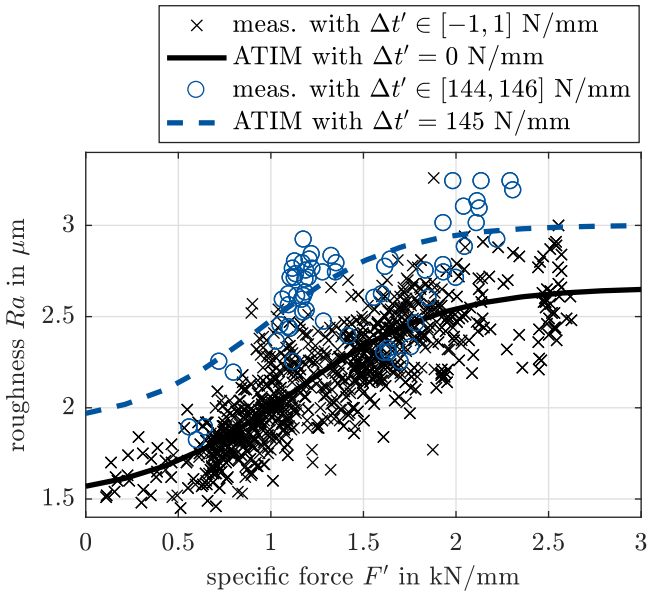

Fig. 10. Depicted is the Asymmetric-Tension Imprint Model (ATIM) evaluated for a specific tension offset of $0\,\mathrm{N\,mm^{-1}}$ and $149\,\mathrm{N\,mm^{-1}}$ respectively. Furthermore, the measurement points are shown, which are within a range of $\pm 1\,\mathrm{N\,mm^{-1}}$ of these values.

since the simultaneously scanned area of the sensor of approximately 150 µm is shorter than the specification of DIN EN ISO 21920-3, which is 0.4 mm to 40 mm [30]. Therefore, we attempted to determine the overall measurement noise of this roughness measurement for DC04 and operating point range. We estimated the noise by measuring the surface roughness of unmoving strip for 30 sec. The standard deviation in this experiment was 0.08 µm for an operating point of $Ra = 2.37$ µm. Additionally, at an alternative operating point of $Ra = 1.51$ µm, we observed a standard deviation of 0.12 µm. After analyzing two more operating points, the standard deviation of the measurement noise for our material (DC04) and process conditions can be conservatively estimated to be between 0.06 µm to 0.13 µm. However, it is important to acknowledge that the modeling of measurement noise is still an open challenge that requires further research.

The ATIM demonstrates close agreement with empirical observations. The overall RMSE across all validation data is 0.202 µm, and the mean error is mean($Ra - Ra_{\mathrm{meas}}$) = 0.0173 µm. Given that measured targets inherently contain sensor noise of 0.06 µm to 0.13 µm, this RMSE reflects an observational error that includes the noise contribution of Ra_{meas}. Consequently, it should be interpreted as an upper bound on the intrinsic model error rather than a denoised estimate of model performance. Another attempt to estimate the model accuracy is to determine the mean value of each grid element, as this can reduce the influence of measurement noise. Subsequently, we can determine the RMSE of the 107 grid elements that sort the 3975 measured and synchronized data points. According to this procedure, we arrive at a noise-reduced RMSE value of 0.0973 µm. It is important to note that some grid elements have only a small number of valid measurement data, which means that the estimated RMSE might not accurately represent true performance. By exclusively selecting grid elements that contain a minimum of 10 measurement points, we arrive at 82 valid grid elements and another estimate of the model accuracy of 0.0861 µm.

Nevertheless, while these results indicate good model performance, a fully rigorous assessment is not possible with the presented experimental data. The available findings remain affected by measurement noise, sample sizes per grid element are uneven, and residual noise characteristics may be heteroscedastic or spatially correlated, all of which can bias error estimates.

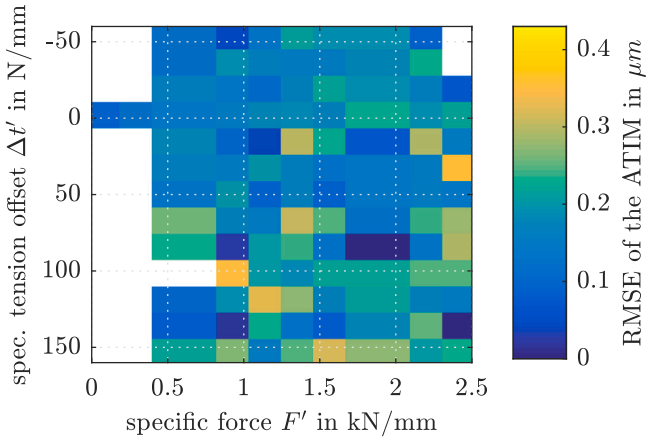

Fig. 11. The Asymmetric-Tension Imprint Model (ATIM) was validated in the input space consisting of the specific force and tension offset using incremental tension offsets of $7.5\,\mathrm{N\,mm^{-1}}$ and specific force increments of $0.5\,\mathrm{kN\,mm^{-1}}$. Additionally, a colormap displays the root mean square error (RMSE) of all measurement points within the corresponding grid element. (For interpretation of the references to color in this figure legend, the reader is referred to the web version of this article.)

5. Thickness-independent roughness control

5.1. Control scheme

To simultaneously control the roughness Ra from the strip thickness h_1, the roll gap height s and the strip tensions t_0, t_1 need to be actuated simultaneously. This is necessary because the resulting roughness and strip thickness are strongly interrelated, affecting both control parameters simultaneously. In the event of an increase in the roll gap height, the rolling force decreases, resulting in an increase in the roll gap deflection. In general, this causes the resulting strip thickness to increase more than the adjusted roll gap height, and it causes the strip roughness to decrease. In the case of a reduction in strip tension, the rolling force increases, causing the roll gap deflection to increase, despite a constant roll gap height. Likewise, the thickness and roughness of the strip are affected.

The necessary roll gap height and tension offset can be determined through the model inversions from cold rolling (see Appendix A), Roll Stand Deflection (see Appendix B), and the ATIM (Section 4). This is necessary because we cannot use the ATIM to calculate the needed roll gap height s directly, instead, we need a different model to predict the needed process forces for a given height reduction and a model to compensate for the force-dependent roll stand deflection.

The subsequently calculated trajectories of the roll gap height s are then provided to a model predictive controller [12], which converts the necessary roll gap height into the position of a spindle and a piezoelectric actuator. This effectively addresses the issue of over-actuation and additionally ensures a balance between the control energy and trajectory tracking.

In Fig. 12, the tension-based control loop is shown in a simplified manner, where the model predictive control is not depicted because it is a rolling-mill-specific modification and is not critical for the control scheme's success. The model-based controller calculates the necessary roll gap height s and strip tensions t_0, t_1, based on the desired strip roughness Ra_{des} and outgoing strip thickness h_{des}, as well as measurable disturbances. The strip width w_0 and strip thickness h_0 can be measured and are modeled as disturbances.

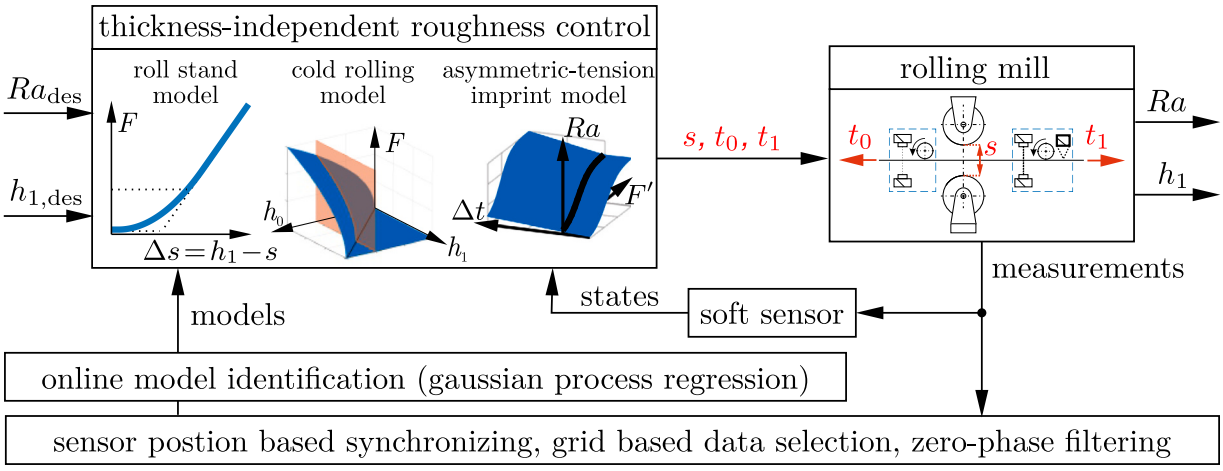

Fig. 12. Depicted is the control loop for independently controlling the strip thickness h_1 and strip mean roughness Ra with the roll gap s and strip tension t_0, t_1. The thickness-independent roughness control uses three process models to calculate the needed roll gap and strip tension. Additionally the process models are identified online using Gaussian process regression and position-based synchronized data.

The model inversion starts by creating a vector of specific strip tension offsets $\boldsymbol{\Delta t'}$ that spans the process range

$$\begin{aligned} &\boldsymbol{\Delta t'} = [\Delta t'_1, \dots, \Delta t'_i, \dots \Delta t'_n] \\ &\quad i \in [1, \dots, n] \\ &\Delta t'_i \in [\Delta t'_{\min}, \Delta t'_{\max}] \quad . \end{aligned} \tag{13}$$

An evaluation at discrete points of the specific strip tension offset is sufficient here, as the underlying models are already provided as discrete characteristic maps by the model identification. Moreover, the characteristic maps exhibit substantial local linearity if key points, such as when the tension offset or height reduction are zero, are sampled.

Next, we can evaluate the Cold Rolling Model (Appendix A) to calculate the rolling force $\boldsymbol{F}$ based on the desired strip thickness h_{des}, measured incoming strip geometry h_0, w_0, and specific strip tension offsets $\boldsymbol{\Delta t'}$:

$$\begin{aligned} &\boldsymbol{F} = [F_1, \dots, F_i, \dots F_n] \\ &F_i = f_S(h_0, w_0, h_1, \Delta t'_i, \boldsymbol{\Theta}_S) \quad . \end{aligned} \tag{14}$$

Then, we can determine the resultant strip roughness $\boldsymbol{Ra}$ based on the ATIM (see (8)) for each pair of specific rolling force $\boldsymbol{F'} = \boldsymbol{F}/w_0$ and the strip tension offset $\boldsymbol{\Delta t'}$:

$$\begin{aligned} &\boldsymbol{Ra} = [Ra_1, \dots, Ra_i, \dots Ra_n] \\ &Ra_i = f_{ti}\left(\frac{F_i}{w_0}, \Delta t'_i, \boldsymbol{\Theta}_{ti}\right) \quad . \end{aligned} \tag{15}$$

Finally, a minimization between the desired roughness Ra_{des} and the vector of resulting roughness values $\boldsymbol{Ra}$ leads to the necessary specific strip tension offset $\Delta t'$, which can be sent to the cold rolling mill:

$$\Delta t'_{opt} = \arg\min_{\Delta t'_i} \left| \boldsymbol{Ra}(\boldsymbol{\Delta t'}) - Ra_{des} \right| \quad . \tag{16}$$

To determine the necessary height of the roll gap s_{opt}, a similar approach can be taken. Based on the roll stand deflection model in Appendix B, the elastic deflection of the stand can be determined. However, the optimized rolling force F_{opt} is necessary, for which the ATIM holds the desired roughness Ra_{des} and specific tension offset $\Delta t'$:

$$Ra_{des} = f_{ti}\left(\frac{F_{opt}}{w_0}, \Delta t'_{opt}, \boldsymbol{\Theta}_{ti}\right) \quad . \tag{17}$$

Subsequently, the roll stand deflection Δs_{opt} can be determined and translated into the necessary roll gap height s_{opt} using (B.1):

$$s_{opt} = h_1 - \Delta s_{opt} = h_1 - f_M(F_{opt}, \boldsymbol{\Theta}_M) \quad . \tag{18}$$

We can also use this model evaluation to determine the maximum possible range in which the two control variables, mean roughness Ra and strip thickness h_1, can be independently controlled from each other. For this, (16) must be replaced by a minimization or maximization of the resulting strip roughness:

$$Ra_{\min} = \min_{\Delta t'_i} \boldsymbol{Ra}(\boldsymbol{\Delta t'}), \quad Ra_{\max} = \max_{\Delta t'_i} \boldsymbol{Ra}(\boldsymbol{\Delta t'}) \quad . \tag{19}$$

5.2. Simulative process analysis

The process window $Ra \in [Ra_{\min}, Ra_{\max}]$ determined for the mean roughness of the strip depends on the incoming strip geometry h_0, w_0 and outgoing strip thickness h_1. For DC04 steel ($w_0 \times h_0$: 8.06 mm×1 mm), the blue area illustrates the resulting process window as a function of outgoing strip thickness h_1 (Refer to Fig. 13 with legend entry "Tension Control"). In other words, the marked area represents a valid combination of mean roughness and outgoing strip thickness that can be controlled by the rolling mill.

Furthermore, we evaluate a Tandem Control scheme for comparison, which we presented in 2023 [9]. Here, two rolling stands were used with distinct roll roughness profiles to independently control the mean roughness Ra from the outgoing strip thickness h_1. The first stand features a smooth surface, whereas the second stand is similar to the one employed in this publication.

In this comparison, it is particularly noticeable that the process window for Tandem Control increases with decreasing outgoing strip thickness h_1. This phenomenon can be attributed to the increase in total forces. Therefore the minimal and maximal possible strip roughness has an increasing likelihood to match the roughness of either roll. In Tandem Control this corresponds either to the smooth roll (Ra_{roll} = 0.8 µm) or the rough roll (Ra_{roll} = 2.38 µm).

Moreover, we observe that the Tension Control process window is highest at low height reductions (h_1 = 1 mm with $\Delta Ra \approx$ 0.33 µm) and is reduced with increasing height reduction (h_1 = 0.96 mm with $\Delta Ra \approx$ 0.21 µm). This can be attributed to the fact that the sensitivity of the ATIM with respect to rolling force and tension offset decreases with increasing rolling force level and the force level increases with a growing height reduction (Fig. 10).

Another important characteristic of roughness control that needs to be investigated is its ability to compensate for process disturbances, e.g. a variation in the incoming strip thickness $h_0 = (1.000 \pm 0.005)$ mm. This corresponds to one third of the strip thickness tolerance permitted by DIN EN 10140 for the precision strips used in these experiments [31]. In this analysis, we assess the model by applying a

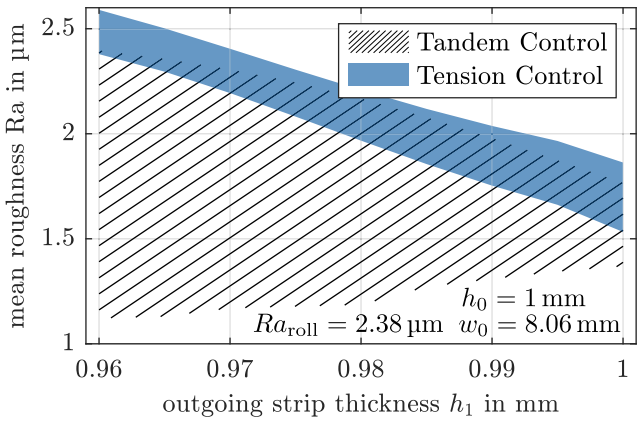

Fig. 13. A comparison of the possible process windows of tandem control from data presented in [9] with the tension-based roughness control presented in this publication. The black hatched area depicts all combinations of the outgoing strip thickness and mean roughness that can be controlled by the tandem control. Equivalently, the blue area refers to the tension control.

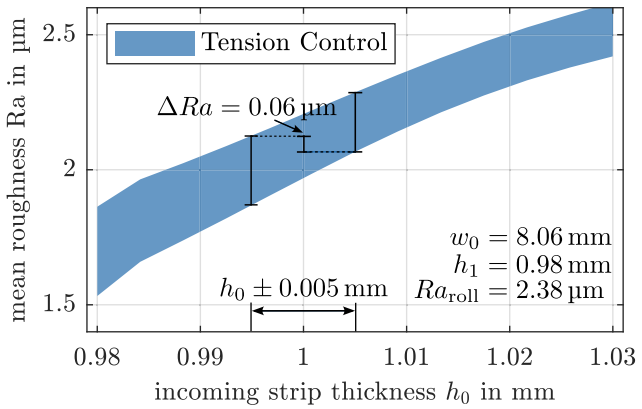

Fig. 14. Depicted is the process window plotted at a constant outgoing strip thickness and varying incoming strip thickness. Furthermore, the reduction of the process window for an exemplary tolerance of the incoming strip of $h_0 = (1.000 \pm 0.005)\,\text{mm}$ is visualized.

predetermined outgoing strip thickness h_1, while subsequently varying the thickness of the incoming strip h_0. The feasible range of strip roughness for each specified operating point is evaluated as a function of the thickness of the incoming strip. To maintain a constant outgoing strip thickness and roughness despite disturbances in the incoming strip thickness, the tension offset needs to be actuated. Therefore it becomes evident that the process window is reduced by the disturbance.

In addition, to address dynamic disturbances, it is essential to confirm that the actuator responds rapidly enough to produce the required tension adjustment. To achieve this, a conservative estimation can be employed, offering an upper threshold for the actuator derivative $\dot{i}_{\text{min}}$ needed to compensate for the disturbance, assuming the process window is compatible with the given disturbance range:

$$\dot{i}_{\text{min}} < \frac{2\Delta t' w_0 v}{\lambda} \quad . \tag{20}$$

Thus, an estimated value of $\dot{i}_{\text{min}} < 2\,\text{kN s}^{-1}$ (or 240 MPa s^{-1} based on the given material geometry) ensues for a disturbance of wavelength $\lambda = 1\,\text{m}$ and a process speed of $v = 50\,\text{m min}^{-1}$. To put this calculation in perspective, this value can still be accomplished with the given lab-scale rolling mill, but would exceed its limits at higher speeds or smaller wavelengths.

Intersecting individual process windows for all possible incoming strip thicknesses identifies the range where the control system is able to independently control the roughness from thickness despite disturbances. For an incoming thickness of $h_0 = (1.000 \pm 0.005)\,\text{mm}$ and an outgoing thickness of $h_1 = 0.98\,\text{mm}$, the intersection of the process windows of $\Delta Ra = 0.06\,\mu\text{m}$ is shown in Fig. 14. Without considering actuator dynamics, Roughness Control can fully counteract disturbances, maintaining consistent strip thickness and roughness. However, we face a limitation, since we can only adjust the roughness by approximately $\Delta Ra = 0.06\,\mu\text{m}$. In comparison, in the absence of disturbances, the roughness can be adjusted by $\Delta Ra = 0.24\,\mu\text{m}$. Controllability differs due to the strong coupling of height reduction with force and strip roughness, which reduces the controllability of the process by 75%.

To counteract this reduction in controllability, the maximum strip tension could be increased further and it is highly advantageous when the incoming strip thickness exhibits as few variations as possible. For example, halving the disturbance of the incoming strip thickness $h_0 = (1.0000 \pm 0.0025)\,\text{mm}$ allows for an intersection of the process windows of $\Delta Ra = 0.15\,\mu\text{m}$. This intersection can also be achieved alternatively by increasing the maximum strip tension by 33% with the original strip thickness disturbance $h_0 = (1.000 \pm 0.005)\,\text{mm}$.

5.3. Experimental process analysis

To experimentally validate the simulative process analysis in Section 5.2, we performed controlled experiments using the same material (DC04, $w_0 \times h_0$: $8.06 \times 1\,\text{mm}$). In these experiments, we determined the appropriate specific tension offset by model inversion; see (19). Subsequently, we determined the relevant strip tensions at the entry and exit using (10)–(11).

We conducted ten experiments using five different outgoing strip thicknesses h_1 and two specific tension offsets $\Delta t'$. We chose specific tension offsets $\Delta t'$ that our model predicted would result in the highest and lowest roughness transfer. We synchronized all data based on sensor positions and used every data point to calculate mean and variance, ensuring that they match the thickness of the outgoing strip (h_1) within a tolerance of 3 µm.

This experimental process analysis is shown in Fig. 15. The blue area represents the process window from the simulative process analysis for an incoming strip geometry of $w_0 = 8.06\,\text{mm}$ and $h_0 = 1\,\text{mm}$. The lower and upper edges correspond to the minimum and maximum possible roughness transfer that is predicted in simulation. In addition, we depict two black curves that represent the minimum Ra_{min} and maximum roughness transfer Ra_{max} that we measured in this experimental analysis. We represent the mean and standard deviation of each individual experiment as an error bar with one standard deviation, and the five experiments that represent the same roughness transfer are connected by a dotted or solid black line, respectively. In theory, the two curves should correspond to the lower and upper edges of the blue process window. However, three discrepancies are noticeable here, which we will explain and discuss in more detail below.

The first notable observation is seen in the outgoing strip thickness $h_1 = 1\,\text{mm}$. Here, the process window predicts a controllable variation in roughness of $\Delta Ra = 0.33\,\mu\text{m}$. However, we could not confirm this in the experiment. Here, the minimum and maximum roughness transfer occurs as $Ra_{\text{min}} = 1.753\,\mu\text{m}$ and $Ra_{\text{max}} = 1.703\,\mu\text{m}$. Since the minimum roughness transfer is greater than the maximum roughness transfer at this operating point, it suggests that no variation in roughness is to be expected at this operating point. This also aligns with expert knowledge, as there is no decrease in height at this operating point, and therefore elastic compression of the material occurs mainly. Nevertheless, there is some roughness transfer since the initial mean roughness Ra_{i-1} is $(1.5 \pm 0.2)\,\mu\text{m}$ and therefore lower than the measured range of 1.703 µm to 1.753 µm. A possible explanation is that individual peaks of the roll surface imprint on the material, causing a local deformation of the material and therefore this phenomenon. The model predicts a controllable process window in contrast to these results due to the

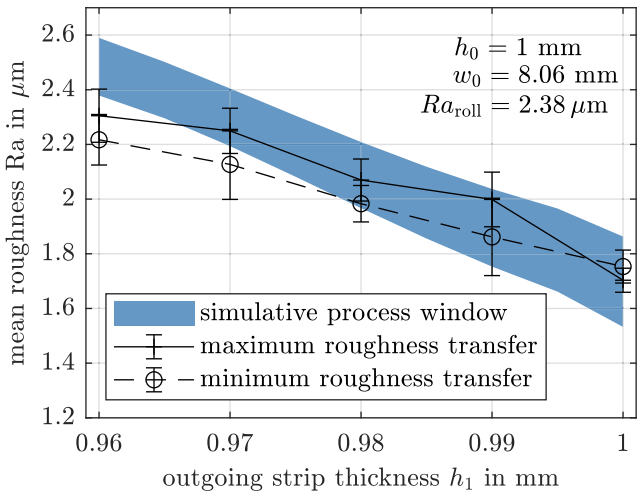

Fig. 15. Depicted is the experimental validation of the predicted process window for incoming strip geometry of $w_0 \times h_0$ with discrepancies in theoretical predictions and experimental results. All error bars are one standard deviation.

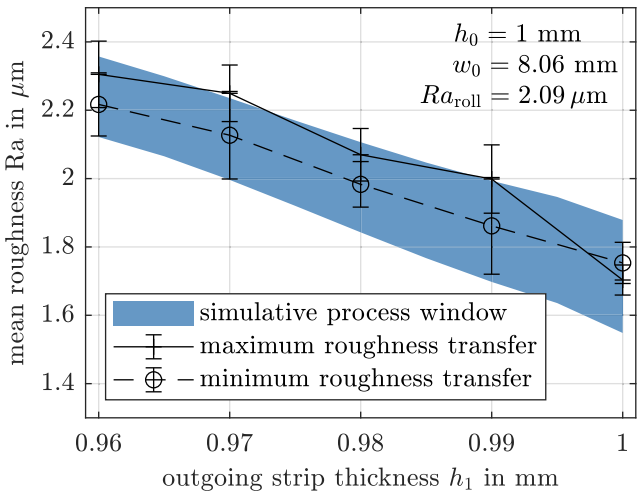

Fig. 16. Depicted is the comparison between the experimental results and a predicted process window based on the updated work roll roughness. All error bars are one standard deviation.

model parameter ΔRa_{init} from the parameter set of the ATIM $\boldsymbol{\Theta}_{\text{ti}}$. This parameter strongly influences the resulting roughness Ra of the strip at low forces F and varying specific strip tension offset $\Delta t'$ and therefore has a substantial influence on the process window.

The second observation is evident when comparing the simulated and experimental process windows for the five operating points. The experimentally determined process window is defined by the difference between the maximum and minimum roughness transfer experiments. It is noticeable that the experimental process window is smaller for all operating points than the simulative process window. Thus, we found a process window of $\Delta Ra = Ra_{\text{max}} - Ra_{\text{min}} = [0.088, 0.123, 0.087, 0.137]$ µm for the operating points $h_1 = [0.96, 0.97, 0.98, 0.99]$ mm. This corresponds to a reduction compared to the simulative process window of [62.3, 49.2, 67.4, 53.82] %. We can explain this deviation between experiment and simulation since we used the assumption that the incoming geometry is constant in the simulation. In the conducted experiments, there was an observed fluctuation in the thickness of the incoming strip h_0 of ±8 µm. This inevitably leads to an increase in uncertainty at the evaluated operating point and a reduction of the measurable process window in reality.

The third notable observation refers to the average value of the process window, which can be calculated as the arithmetic mean of the minimum and maximum roughness transfer.

$$Ra_{\text{avg}} = \frac{Ra_{\text{min}} + Ra_{\text{max}}}{2} \quad . \tag{21}$$

This average process window shows ever-greater deviations between the measured and simulated values. Thus, for an outgoing strip thickness $h_1 = 0.96$ mm, the simulation predicts an average mean roughness $Ra_{\text{avg}} = 2.48\,\mu$m. However, the experimental validation yielded an average mean roughness of 2.26 µm. This indicates that the roughness predicted in the simulation can no longer be achieved in the experiments, as the roughness of the roll has been reduced due to wear. We can also confirm this hypothesis, as we measured the roll roughness using a rubber mold and a Keyence-VHX 7000 digital microscope after these experiments, resulting in a roughness of 2.09 µm.

We selected two different positions on the work roll and created rubber replicas, labeled B1 and B2. For each replica, roughness values were measured at five different locations along the rolling direction and five locations along the transverse direction (see Table 4). The high deviations between the different locations of the roughness measurement can be attributed, on the one hand, to the EDT process, since we were promised a tolerance of the resulting surface roughness of ±10%. On the other hand, uneven wear of the roll surface can also be attributed to issues such as eccentricities of the roll. These uneven areas can be a result of increased or reduced rolling forces that depend on the roll angle.

Table 4
Measurement of roll roughness using rubber mold and Keyence-VHX 7000 digital microscope.

	Horizontal		Vertical	
Sample	B1	B2	B1	B2
Measurement in µm	2.13	2.12	1.89	2.08
	1.91	2.09	2.01	2.01
	2.21	2.29	2.1	2.17
	2.11	2.22	2.08	2.09
	1.95	1.9	2.16	1.91
Average in µm	2.06	2.12	2.05	2.05
Std Dev in µm	0.13	0.15	0.1	0.1
Average in µm	2.09			

The roll wear is attributed to rolling tests conducted outside of this publication, between the results from Sections 4.2 and 5.3. In Fig. 16, we compared experimental data with a new cold rolling simulation using the updated roll roughness of $Ra_{\text{roll}} = 2.09$ µm. Here, we observe a notable improvement between the predicted process windows and the experimental data. Furthermore, the ATIM shows good extrapolation behavior for process parameters that were not previously observed since it was able to predict the new surface imprinting of the worn work rolls.

6. Conclusion

In this study, we presented a multiscale simulation and control framework for skin-pass rolling that addresses the challenges of simultaneously attaining desired strip thickness and surface roughness using a single roll stand. By employing a hierarchical modeling structure that combines macroscopic and mesoscopic simulations, the study successfully demonstrates how surface roughness and imprint during rolling are affected by thickness reduction and asymmetric strip tension.

The innovative use of an optimized Fourier series representation to model surface profiles has led to improved simulation accuracy. Experimental validation using a laboratory strip rolling mill confirmed that the multiscale modeling technique provides strong predictive capability under asymmetric tensions for DC04 and DC05 steels. Moreover, the

simulation results indicate that asymmetric tension has a high potential to act as an additional actuator for controlling surface roughness without affecting the final strip thickness.

Furthermore, we developed and validated an Asymmetric-Tension Imprint Model to predict the surface roughness of metallic strips during the skin-pass rolling process in real time. Our Asymmetric-Tension Imprint Model accounts for variations in strip tension and rolling force and was experimentally validated using DC04 steel strips in a laboratory setup. The results demonstrated that our model accurately predicts the mean surface roughness with minimal root mean square error (RMSE = 0.202 µm). It does so as a function of the incoming strip roughness Ra_{init}, the roll roughness Ra_{roll}, and material-specific parameters. The model showcases robustness against overfitting and the ability to adapt to various roll surfaces, materials and work roll wear.

Additionally, we introduced a new control strategy to simultaneously control the strip thickness and surface roughness by adjusting roll gap height and asymmetric strip tension through model inversion techniques. Experimental data confirmed the potential of this control method. However, the control approach showed that the process window is substantially smaller than in classical control approaches such as tandem cold rolling with two rolling stands and distinct roll surfaces. The process window denotes the range that allows for roughness adjustment while maintaining a consistent outgoing strip thickness. Thus, the process window in the presented thickness-independent roughness control decreases with increasing height reduction, whereas it increases in tandem cold rolling.

Secondly, it shows major disadvantages when it comes to controlling under disturbances such as the incoming strip thickness. Here, even with small process fluctuations of ±5 µm micrometers, a reduction in the process window of approximately 75% is observed, depending on the operating point. This can be counteracted by increasing the maximum strip tension. However, this approach rapidly encounters the limits of practical applicability, as industrial rolling mills rarely operate beyond tensile stresses of 200 MPa, or the material's yield strength is often reached. In conclusion, adjusting strip roughness using strip tension in a single roll stand quickly becomes impractical, achieving only minor roughness variations in materials like DC04 by 0.15 µm at 207 MPa.

Moreover, effective mitigation of dynamic disturbances requires sufficiently fast actuation. For typical lab conditions with $\lambda = 1\,\mathrm{m}$ *and* $v = 50\,\mathrm{m\,min^{-1}}$, this yields an upper bound of 2 kN $\mathrm{s^{-1}}$, equivalent to approximately 240 $\mathrm{MPas^{-1}}$ for the given geometry. Although achievable on our lab-scale mill, such rates become limiting at higher line speeds or shorter disturbance wavelengths, further constraining practical applicability.

However, the developed Asymmetric-Tension Imprint Model can be used to incorporate strip tension as a supporting actuator into a control loop, where strip tension is only used to counteract effects such as roll wear that reduce the resulting strip roughness *Ra* during operation. Using this method, a limitation in the actuator dynamics of the strip tension does not influence the control quality of the roughness, and this method could potentially extend the lifespan of the textured work rolls. However, an online adaptation of the Asymmetric-Tension Imprint Model is recommended for data-driven monitoring of roll wear. Here, [9] can be used as an example, where we developed a model to predict the roughness of the strip as a function of the rolling pass schedule using Gaussian process regression and expert knowledge.

Beyond the immediate case study of DC04 steel in a single-step rolling environment, our findings offer broader insights into tension-based surface control for metal forming processes. First, the presented multiscale simulation method provides a systematic framework for linking microscopic roughness behavior with macroscopic process variables. Such an approach is generally applicable to other rolling and metal-forming processes where contact conditions, micro topographies, or tension asymmetries are essential. Second, the Asymmetric-Tension Imprint Model, with predictive capacity in real time, opens new avenues for adaptive process control across diverse material grades, rolling stand configurations, or textured roll surfaces. In particular, incorporating strip tension as a supporting actuator to counteract roll wear can extend roll lifetimes and enable consistent surface quality. An online adaptation of the ATIM, as seen in related data-driven approaches, would further refine and generalize its capabilities for industrial deployment.

CRediT authorship contribution statement

Christopher Schulte: Writing – review & editing, Writing – original draft, Visualization, Validation, Software, Methodology, Investigation, Formal analysis, Data curation, Conceptualization. **Xinyang Li:** Writing – original draft, Methodology, Conceptualization. **Mengmeng Zhang:** Writing – review & editing, Visualization, Validation, Software. **David Bailly:** Writing – review & editing, Project administration, Funding acquisition. **Heike Vallery:** Writing – review & editing, Supervision. **Sebastian Stemmler:** Writing – review & editing, Supervision, Project administration, Funding acquisition.

Declaration of competing interest

The authors declare that they have no known competing financial interests or personal relationships that could have appeared to influence the work reported in this paper.

Acknowledgments

This work was supported by the German Research Foundation (DFG, grant no. 424333859).

Appendix A. Cold rolling model

The Cold Rolling Model describes the material forming in the roll gap. Here, the rolled material is fed through the roll gap with the aid of friction and is reduced in thickness. As a consequence of the forces that arise, elastic deformation of the work rolls occurs, resulting in roll deflection and roll flattening ([32], pp. 172–176). This increases the contact area between the roll and the strip, which in turn influences the contact stress profile.

To calculate the force with the model, an approximation of the contact stress profile is applied, which subsequently leads to the process force by integrating the contact stress over the vertically projected contact area [33]. Here, for example, the models according to Kármán [34], Bland and Ford [14] or Alexander [35] can be mentioned, which assume a plane and homogeneous deformation. However, they vary in terms of their model quality and the computation time required, which is increasing in the mentioned order [36].

Furthermore, the neutral plane should be emphasized, as it describes the change in sign of friction between the roll and the strip. On the inlet side of the neutral plane, the roll moves faster than the strip (lead zone), and on the outlet side, the strip moves faster than the roll (lag zone) [13]. An example contact stress curve and the neutral plane with the lead and lag zone is shown in Fig. A.17. Additionally, the geometry of the roll gap with contact angle

$$\alpha_c = \arccos\left(1 - \frac{h_0 - h_1}{2R}\right) \approx \sqrt{\frac{h_0 - h_1}{R}} \tag{A.1}$$

and contact length l_c is shown, where the initial material height h_0 is first reduced to $\hat{s}$ and then elastically recovers to the final strip height h_1.

In this work, the model developed by Bland and Ford [14] is used to determine a prior estimate of the rolling force F as a function f_S of process parameters $\boldsymbol{\Theta}_S$ such as the stiff work roll radius R, yield curve

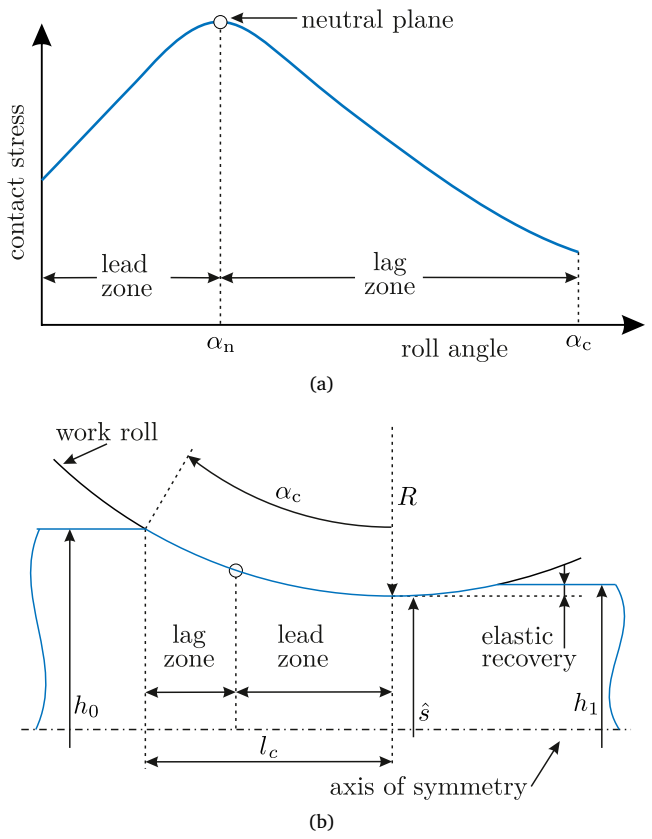

Fig. A.17. Depicted is the contact stress of the roll gap plotted over the roll angle (a) along with the geometric approximation of the roll gap (b). The neutral plane with angle α_n is the point with no relative movement of the work roll and strip and thus separates the lead zone from the lag zone.
Source: Adapted from Orowan ([32], p. 165) and Stockert et al. [13].

$k_f(\alpha)$, coefficient of friction μ, and process variables such as the initial strip geometry h_0, w_0, resultant thickness h_1 and strip tension t_0, t_1:

$$F = f_S(h_0, w_0, h_1, t_0, t_1, \boldsymbol{\Theta}_S) \tag{A.2}$$

$$= 1.15\, w_0\, R \left[\int_0^{\alpha_n} \frac{k_f(\alpha)\, h(\alpha)}{h_1} \left(1 - \frac{t_1}{k_f(0)}\right) \exp\left(\mu X(\alpha)\right) d\alpha \right.$$

$$\left. + \int_{\alpha_n}^{\alpha_c} \frac{k_f(\alpha)\, h(\alpha)}{h_0} \left(1 - \frac{t_0}{k_f(\alpha_c)}\right) \exp\left(\mu \left(X(\alpha_c) - X(\alpha)\right)\right) d\alpha \right] \tag{A.3}$$

with the auxiliary variable

$$X(\alpha) = 2\sqrt{\frac{R}{h_1}} \arctan\left(\sqrt{\frac{R}{h_1}}\right) \alpha \tag{A.4}$$

and angle-dependent thickness

$$h(\alpha) = h_1 + 2R(1 - \cos(\alpha)) \quad . \tag{A.5}$$

To further improve the accuracy of the model, we can take into account the flattening effect on the work rolls caused by the rolling force F. To do this, we can iteratively solve the function call $F = f_S(h_0, w_0, h_1, t_0, t_1, \boldsymbol{\Theta}_S)$ with a flattened roll radius R' that itself is a function of the stiff roll radius R, estimated force F, strip geometry and model parameters $\boldsymbol{\Theta}_S$ according to Hitchcock [37].

Appendix B. Roll stand deflection model

The Roll Stand Deflection Model describes the roll stand and its deflection under load. In literature, various strategies have been documented for adjusting the roll stand deflection model. Although the roll stand deflection model is typically treated as having progressive characteristics, it is worth noting that the effect of the force on the deflection is primarily represented as linear, as seen in [38–40]. However, the roll stand deflection resembles a progressive spring that only behaves linearly for high rolling forces above a threshold force and for static operations, as discussed in [41].

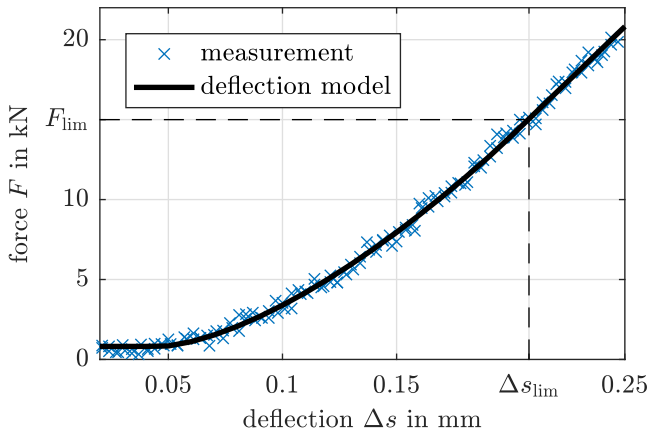

Fig. B.18. Offline identified roll stand deflection model without a metallic strip inside the roll stand, resulting in a deflection $\Delta s = 0 - s$, cf. [17].

The elastic deflection Δs corresponds to the difference between the actual height of the roll gap during load $\hat{s}$ and the height of the initial roll gap without load s. Neglecting the elastic recovery of the material, it is possible to approximate the elastic deflection Δs of the stand as follows:

$$\Delta s = \hat{s} - s \approx h_1 - s \quad . \tag{B.1}$$

The elastic recovery of the material after the roll gap can be neglected due to the high Young's modulus of the material and the low material thickness (cf. [17]). Since the threshold force F_{lim} after which the roll stand deflects linearly is usually not exceeded during skin-pass rolling, a linearization of the process is not admissible. For this reason, a nonlinear model was developed in [17] to fully represent the progressive behavior of the roll stand. The roll stand deflection is modeled as a function $\Delta s = f_M(F, \boldsymbol{\Theta}_M)$, which takes the rolling force F and a set of five process parameters $\boldsymbol{\Theta}_M$ as inputs. These parameters include the mill calibration error F_{calib}, threshold force F_{lim}, roll stand deflection at the threshold force Δs_{lim}, the degree of nonlinearity e, and the linear roll stand stiffness m (refer to Table B.5):

$$\Delta s = \begin{cases} \dfrac{F - F_{lim}}{m} + \Delta s_{lim} & F_i > F_{lim} \\ \left(\dfrac{(F - F_{calib})}{c_1}\right)^{\frac{1}{e}} + c_2 & \text{otherwise} \\ c_2 & F \le F_{calib} \end{cases} , \tag{B.2}$$

with the parameters

$$c_1 = \frac{F_{lim} - F_{calib}}{(\Delta s_{lim} - c_2)^e} \quad , \tag{B.3}$$

$$c_2 = \frac{(F_{calib} - F_{lim})\, e}{m} + \Delta s_{lim} \quad . \tag{B.4}$$

An experiment was conducted in which no material was present in the roll gap. This results in the elastic deflection Δs being directly measurable since the roll gap under load $\hat{s}$ corresponds to zero. The resulting roll stand deflection curve is shown in Fig. B.18, and the progressive character of the characteristic curve is particularly noteworthy.

Table B.5
Model parameters of the roll stand deflection model $\boldsymbol{\Theta}_{\mathrm{M}}$, compare [17].

Variable	Value	Description
F_{lim}	15 kN	Minimal, linear force
F_{calib}	0.2 kN	Calibration error
m	137 kN mm^{-1}	Roll stand stiffness
e	1.531	Degree of nonlinearity
Δs_{lim}	0.208 mm	Deflection at F_{lim}

Data availability

The dataset can be accessed and downloaded from the following link: https://github.com/Don-Chris/data_set_roughness_control_in_cold_rolling.

References

[1] Bhav Singh B, Sivakumar K, Balakrishna Bhat T. Effect of cold rolling on mechanical properties and ballistic performance of nitrogen-alloyed austenitic steels. Int J Impact Eng 2009;36(4):611–20. http://dx.doi.org/10.1016/j.ijimpeng.2008.07.082.

[2] Emmens WC. The influence of surface roughness on friction. In: Proceeding 15th congress of international deep drawing research group. IDDRG, 1988, p. 63–70.

[3] Kijima H. Influence of roll radius on contact condition and material deformation in skin-pass rolling of steel strip. J Mater Process Technol 2013;213(10):1764–71. http://dx.doi.org/10.1016/j.jmatprotec.2013.04.011.

[4] Scheers J, Vermeulen M, de Mare C, Meseure K. Assessment of steel surface roughness and waviness in relation with paint appearance. Int J Mach Tools Manuf 1998;38(5–6):647–56.

[5] Li X, Schulte C, Zhu R, Abel D, Hirt G. Modeling and control of tribological properties for subsequent forming process in skin-pass rolling. Mater Res Proc 2023;28:2115–25. http://dx.doi.org/10.21741/9781644902479-226.

[6] Çolak B, Kurgan N. An experimental investigation into roughness transfer in skin-pass rolling of steel strips. Int J Adv Manuf Technol 2018;96(9):3321–30. http://dx.doi.org/10.31466/kfbd.1289221.

[7] Kijima H. Influence of roll radius on roughness transfer in skin-pass rolling of steel strip. J Mater Process Technol 2014;214(5):1111–9. http://dx.doi.org/10.1016/j.jmatprotec.2013.12.019.

[8] Wiklund O, Sandberg F, Lenard JG. Modelling and control of temper rolling and skin pass rolling. In: Metal forming science and practice. 2002, p. 313–43.

[9] Schulte C, Li X, Stemmler S, Vallery H, Hirt G, Abel D. Adaptive pass scheduling for roughness control in cold rolling. IFAC-PapersOnLine (22nd IFAC World Congress) 2023;56(2):2683–8. http://dx.doi.org/10.1016/j.ifacol.2023.10.1360.

[10] Li R, Zhang Q, Zhang X, Yu M, Wang B. Control method for steel strip roughness in two-stand temper mill rolling. Chin J Mech Eng 2015;28(3):573–9. http://dx.doi.org/10.3901/CJME.2015.0310.027.

[11] Bozhkov AI, Kovalev DA, Orekhov ME, Degtev SS, Chereshnev VV. Controlling the surface roughness of cold-rolled strip. Part 1. Steel Transl 2017;47(10):691–4. http://dx.doi.org/10.3103/S0967091217100023.

[12] Wehr M, Stockert S, Abel D, Hirt G. Model predictive roll gap control in cold rolling with piezoelectric actuators. In: 2018 IEEE conference on control technology and applications. CCTA, Piscataway, NJ: IEEE; 2018, p. 1377–82. http://dx.doi.org/10.1109/CCTA.2018.8511333.

[13] Stockert S, Wehr M, Lohmar J, Abel D, Hirt G. Assessment of flat rolling theories for the use in a model-based controller for high-precision rolling applications. In: AIP conference proceedings. vol. 1896, 2017, 190005. http://dx.doi.org/10.1063/1.5008218.

[14] Bland DR, Ford H. The calculation of roll force and torque in cold strip rolling with tensions. Proc Inst Mech Eng 1948;159(1):144–63. http://dx.doi.org/10.1243/PIME_PROC_1948_159_015_02.

[15] Wehr M, Stenger D, Schätzler S, Beyer R, Abel D, Hirt G. Online model adaptation in cold rolling for improvement of thickness precision. In: 21st IFAC world congress. 2020, http://dx.doi.org/10.1016/j.ifacol.2020.12.2776.

[16] Huber PJ. Robust estimation of a location parameter: The annals of mathematical statistics, 35(1), 73-101. Ann Math Stat 1964;35(1):73–101. http://dx.doi.org/10.1214/AOMS/1177703732.

[17] Schulte C, Li X, Abel D, Hirt G. High precision thickness control in a cold rolling mill using a non-linear roll stand deflection model. Eur Control Conf (ECC) 2021;1907–12. http://dx.doi.org/10.23919/ECC54610.2021.9655117.

[18] Kouzoupis D, Quirynen R, Girrbach F, Diehl M. An efficient SQP algorithm for moving Horizon estimation with Huber penalties and multi-rate measurements. In: 2016 IEEE conference on control applications. CCA, 2016, p. 1482–7. http://dx.doi.org/10.1109/CCA.2016.7588010.

[19] Moreas G, Schyns M. Method and device for the online determination of the micrometric topography of moving products. Centre de Recherches Metallurgiques; 2012, patent number EP 1 806 558 B1.

[20] Schulte C, Li X, Abel D, Hirt G. Model-based control of the strip roughness in cold rolling. IFAC-PapersOnLine (6th IFAC Work Min Miner Metal Process MMM 2021) 2021;54(11):109–14. http://dx.doi.org/10.1016/j.ifacol.2021.10.059.

[21] Li X, Schulte C, Abel D, Teller M, Hirt G, Lohmar J. Modeling and exploiting the strip tension influence on surface imprinting during temper rolling of cold-rolled steel. Adv Ind Manuf Eng 2021;3:100045. http://dx.doi.org/10.1016/j.aime.2021.100045.

[22] Hojda S. Beitrag zur modellierung und simulation des nachwalzens von aluminiumlegierungen für die automobilaußenhaut; 1. Auflage. Umformtechnische schriften, vol. 204, Aachen, german: Verlagshaus Mainz GmbH, RWTH Aachen University; 2020, Dissertation.

[23] International Organization for Standardization. ISO 21920-2: Geometrical product specifications (GPS) - Surface texture: Profile - Part 2: Terms, definitions and surface texture parameters. 2022-12, http://dx.doi.org/10.31030/3294017.

[24] Abbott EJ. Specifying surface quality a method based on accurate measurement and comparison. Mech Eng 1933;55:569–72, URL https://cir.nii.ac.jp/crid/1570854175294365824.

[25] Johnson KL. Contact mechanics. 9th ed.. Cambridge: Cambridge Univ. Press; 2003, http://dx.doi.org/10.1017/CBO9781139171731.

[26] Zahara E, Kao Y-T. Hybrid Nelder–Mead simplex search and particle swarm optimization for constrained engineering design problems. Expert Syst Appl 2009;36(2):3880–6. http://dx.doi.org/10.1016/j.eswa.2008.02.039.

[27] Nelder JA, Mead R. A simplex method for function minimization. Comput J 1965;7(4):308–13. http://dx.doi.org/10.1093/comjnl/7.4.308.

[28] Kennedy J, Eberhart R. Particle swarm optimization. In: 1995 IEEE international conference on neural networks. New York and Piscataway, NJ: Institute of Electrical and Electronics Engineers; 1995, p. 1942–8. http://dx.doi.org/10.1109/ICNN.1995.488968.

[29] AMEPA Angewandte Messtechnik und Prozessautomatisierung GmbH. Messunsicherheit des SRM und Bestimmung des Messunsicherheitsbudgets nach GUM bzw. EU-richtlinie EAL-R4, german; 2012, [Received on 17 June 2025] available on request.

[30] International Organization for Standardization. ISO 21920-2: Geometrical product specifications (GPS) – Surface texture: Profile - Part 3: Specification operators. 2022, http://dx.doi.org/10.31030/3294017.

[31] DIN Deutsches Institut für Normung eV. DIN EN 10140:2006-09: Cold rolled narrow steel strip – Tolerances on dimensions and shape. 2006, http://dx.doi.org/10.31030/9708467.

[32] Orowan E. The calculation of roll pressure in hot and cold flat rolling. Proc Inst Mech Eng 1943;150(1):140–67. http://dx.doi.org/10.1243/PIME_PROC_1943_150_025_02.

[33] Wehr M. Self-optimizing automatic gauge control in high precision cold rolling with piezoelectric actuators [Ph.D. thesis], RWTH Aachen University; 2021, http://dx.doi.org/10.18154/RWTH-2021-04118.

[34] von Kármán T. On the theory of rolling. Z Angew Math Mech 1925;2:139–41. http://dx.doi.org/10.1098/rspa.1972.0025.

[35] Alexander JM. On the theory of rolling. Proc R Soc A: Math Phys Eng Sci 1972;326(1567):535–63. http://dx.doi.org/10.1098/rspa.1972.0025.

[36] Schätzler SM. Verbesserung der Formtoleranzen kaltgewalzter Spaltbänder durch eine piezoelektrisch unterstützte Walzspaltregelung [Ph.D. thesis], Aachen: RWTH Aachen University; 2021, http://dx.doi.org/10.18154/RWTH-2021-10367, Medium: online, German.

[37] Hitchcock JH. Elastic deformation of rolls during cold rolling. ASME Rep Spec Res Comm Roll Neck Bear 1935;33:33–41.

[38] Ginzburg VB, Ballas R. Flat rolling fundamentals. Manufacturing engineering and materials processing, vol. 57, Dekker, New York, NY; 2000.

[39] Lenard JG. Primer on flat rolling, 2nd ed.. Elsevier insights, Burlington: Elsevier Science; 2013.

[40] Kopp R, Wiegels H. Einführung in die Umformtechnik: (in german). 2nd ed.. Verl. Mainz, Aachen; 1999.

[41] Roberts. Cold rolling of steel. Manufacturing engineering and materials processing, vol. v. 2, New York: CRC Press; 1978, http://dx.doi.org/10.1201/9781315139661.